


## Numerical calculation of the particle–fluid–particle stress in random arrays of fixed particles

Min Wang 

*Fluid Dynamics and Solid Mechanics Group, Theoretical Division, Los Alamos National Laboratory,  
Los Alamos, New Mexico 87545, USA*

Yunchao Yang

*Department of Mechanical and Aerospace Engineering, University of Florida, Gainesville,  
Florida 32611, USA*

Duan Z. Zhang \*

*Fluid Dynamics and Solid Mechanics Group, Theoretical Division, Los Alamos National Laboratory,  
Los Alamos, New Mexico 87545, USA*

S. Balachandar

*Department of Mechanical and Aerospace Engineering, University of Florida, Gainesville,  
Florida 32611, USA*



(Received 25 January 2021; accepted 6 October 2021; published 22 October 2021)

Based on the nearest particle statistics [Zhang, *J. Fluid Mech.* **910**, A16 (2021)], the phase interaction force in a multiphase flow is decomposed into a particle–mean-field force and the divergence of the particle–fluid–particle (PFP) stress. The PFP stress is proportional to the correlation product of the distance from a particle to its nearest neighbor and the force on the particle conditionally averaged on the nearest-neighbor location. In this work, a functional form of the stress is obtained corrected to the first order of the ratio between the interparticle distance and the macroscopic length scale of the flow. Particle-resolved numerical simulations are used to calculate the PFP stress in random arrays of fixed particles and to explore the physics represented by the stress. The numerical results show that the PFP stress is attractive along the direction of the flow and is repulsive in the directions perpendicular to the flow. In the flow regime simulated, this PFP stress can be considered as a macroscopic representation of the drafting–kissing–tumbling mechanism. The Reynolds stress for the fluid phase is also calculated and compared with the PFP stress.

DOI: [10.1103/PhysRevFluids.6.104306](https://doi.org/10.1103/PhysRevFluids.6.104306)

### I. INTRODUCTION

In many engineering calculations of multiphase flows, drag force is the primary force considered between the phases. Effects of particle volume fraction, Reynolds number, and Mach number have been considered in drag force models [1–7]. Spatial inhomogeneity is not usually considered in the models. It is now known [8–10] that such force models are insufficient, and particle–fluid–particle (PFP) interactions in an inhomogeneous flow need to be considered. The lack of representation of mean-field gradient has also been pointed out by Lhuillier [11] for Stokesian suspensions. Nott *et al.* [12] showed that in a Stokesian suspension, the viscous force on a particle can be written as a sum

---

\*dzhang@lanl.gov

of forces from the particles in the suspension. The multiparticle interaction is represented by the resistance coefficients. The force on a particle can be decomposed as effective pair interactions, and then a particle phase stress, similar to the virial stress in molecular dynamics, can be defined based on the Taylor expansion of the weighting function [12,13] in the volume average. The phase interaction force in a Stokesian suspension is then expressed as a drag force plus a divergence of the particle phase stress. However, as pointed out by the authors, such force decomposition and the stress definition are only valid for Stokes flows and are not valid for flows with finite Reynolds numbers. Given that the drag force in a linear inhomogeneous Stokesian suspension needs to be supplemented with a divergence of a stress, there is reason to expect that a similar stress also exists and plays an important role in a multiphase flow with a finite Reynolds number.

Furthermore, it is known that an average drag force model does not sufficiently describe formation of mesoscale structures [14,15] and their dynamics, such as the drafting–kissing–tumbling motions [16,17] among the particles. The macroscopic models representing these mesoscale mechanisms have not been well studied. A force vector can only be used to represent the phase interaction in a certain direction, while mesoscale particle structures formed by PFP interactions are three-dimensional objects. The deformation and evolution of a three-dimensional object need to be described by a tensor. A stress tensor is needed to drive their motions. Fox *et al.* [9,10] proposed a two-fluid model based on kinetic theory and showed that a stress accounting for fluid mediated particle interactions, or PFP interactions, is needed for the hyperbolicity of the equations. How to define such a stress in a general multiphase flow is a challenging modeling issue. Adding to the difficulty is the long-range hydrodynamic interactions among the particles in a disperse multiphase flow that often result in divergent integrals in the study of effective quantities. In a linear system, the renormalization method has been used by Batchelor [18], Batchelor and Green [19], and Jeffrey [20] to calculate the average quantities in the dilute particle limit. Its extension to finite volume fractions and nonlinear problems has not been successful.

With many recent developments on computer technologies and numerical methods, many particle-resolved calculations have been performed [21–27]. In principle, the numerical results contain all the information about particle interactions in the multiphase flow, including that needed to define and calculate the stress. The question about the stress can also be asked from the point of view of the numerical simulations. What else can we learn from the numerical results other than calculating the drag force between the phases? The present work shows that the numerical results can be further processed to obtain the PFP stress, which represents macroscopic effect of drafting–kissing–tumbling motions at the interparticle scale.

To extract more physical understanding from the particle-resolved numerical results and to study PFP interactions, one needs a mathematical tool capable of handling long-range interactions, applicable to finite particle volume fractions, and nonlinear systems. Recently, it is shown [28,29] that the divergence difficulty that arises from the long-range particle interactions can be bypassed by using quantities conditionally averaged on the nearest particle. Averages thus calculated account for effects from all particles in the flow, not only the binary interaction between the nearest pair. Similarly to the work of Nott *et al.* [12], the phase interaction force is decomposed into a particle–mean-field force and a divergence of the PFP stress. The averaging method, the force decomposition, and the PFP stress definition are valid for multiphase flows with finite particle volume fractions and finite Reynolds numbers.

The PFP stress is defined in a similar form as the virial stress [30] in particulate systems, but with the related distances and the forces replaced by the corresponding quantities from the nearest particle statistics to avoid the divergence difficulties from long-range particle interactions. The main objective of the present paper is to numerically calculate the PFP stress and then study the physics represented by it and the consequence for multiphase flow models. In the next section, the newly developed nearest particle statistics and the PFP stress [28,29] are introduced, with details explained in the Appendix. Section III describes the preparation of the

statistical samples and the numerical simulations. In Sec. IV, we use the ergodicity principle to calculate the PFP stress, an ensemble averaged quantity, as a volume average in statistically uniform flows and then study its properties. Although the main objective of this paper is to study the PFP stress, the numerical results produced can also be used to calculate the fluid Reynolds stress. Such calculated Reynolds stress are then compared to the PFP stress in Sec. IV.

## II. PHASE INTERACTION FORCE AND THE PFP STRESS

### A. The phase interaction force

To clarify the role of the PFP stress in a multiphase flow model, we start by listing the averaged momentum equations of a two-fluid model obtained from the ensemble phase averaging method [31–33]. They are

$$\frac{\partial}{\partial t}(\theta_f \rho_f \mathbf{v}_f) + \nabla \cdot (\theta_f \rho_f \mathbf{v}_f \mathbf{v}_f) = \theta_f \nabla \cdot \boldsymbol{\sigma}_f + \nabla \cdot (\theta_f \boldsymbol{\sigma}_f^{\text{Re}} + \theta_p \bar{\mathbf{T}}_f) - n_p \bar{\mathbf{f}}_{\text{pf}}, \quad (1)$$

$$\frac{\partial}{\partial t}(\theta_p \rho_p \mathbf{v}_p) + \nabla \cdot (\theta_p \rho_p \mathbf{v}_p \mathbf{v}_p) = \theta_p \nabla \cdot \boldsymbol{\sigma}_f + \nabla \cdot (\theta_p \boldsymbol{\sigma}_p^{\text{Re}}) + n_p \bar{\mathbf{f}}_{\text{pf}}, \quad (2)$$

where subscripts  $f$  and  $p$  denote the fluid and particle phases respectively,  $\rho$  is the material density of the corresponding phase,  $\theta$  is the volume fraction,  $\mathbf{v}$  is the average velocity,  $\boldsymbol{\sigma}_f$  is the average fluid stress,  $\boldsymbol{\sigma}^{\text{Re}}$  is the stress due to velocity fluctuations of the corresponding phase,  $\bar{\mathbf{T}}_f$  is the average stress in the fluid phase caused by phase interactions at the length scale of the particle size,  $n_p$  is the particle number density, and  $\bar{\mathbf{f}}_{\text{pf}}$  is the average of phase interaction force per particle. In a flow configuration  $\mathcal{C}$ , for a particle at position  $\mathbf{x}$  and time  $t$ , the phase interaction force  $\mathbf{f}_{\text{pf}}$  and the stress  $\mathbf{T}_f$  is defined as [31,32]

$$\mathbf{f}_{\text{pf}}(\mathbf{x}, t; \mathcal{C}) = \oint [\boldsymbol{\sigma}_s(\mathbf{z}, t; \mathcal{C}) - \boldsymbol{\sigma}_f(\mathbf{z}, t)] \cdot \mathbf{n} dS_z, \quad (3)$$

and

$$\mathbf{T}_f(\mathbf{x}, t; \mathcal{C}) = \frac{1}{V_p} \oint (\mathbf{z} - \mathbf{x}) [\boldsymbol{\sigma}_s(\mathbf{z}, t; \mathcal{C}) - \boldsymbol{\sigma}_f(\mathbf{z}, t)] \cdot \mathbf{n} dS_z, \quad (4)$$

where  $V_p$  is the particle volume,  $\boldsymbol{\sigma}_s(\mathbf{z}, t; \mathcal{C})$  is the fluid stress on the surface location  $\mathbf{z}$  of the particle centered at position  $\mathbf{x}$  at time  $t$ ,  $\boldsymbol{\sigma}_f(\mathbf{z}, t)$  is the average fluid stress, and  $\mathbf{n}$  is the outward unit normal of the surface element  $dS_z$  on the particle. The overbars on  $\bar{\mathbf{f}}_{\text{pf}}$  and  $\bar{\mathbf{T}}_f$  in (1) and (2) denote the averages over all the configurations in which  $\mathbf{x}$  is occupied by a particle center. Although the stress  $\bar{\mathbf{T}}_f$  is of interest and computable using particle-resolved numerical simulations, the present work only focuses on the phase interaction force  $\bar{\mathbf{f}}_{\text{pf}}$ .

The product  $n_p \bar{\mathbf{f}}_{\text{pf}}$  in (1) and (2) is the force density appearing in the momentum equations for both phases with opposite signs. Those equations do not explicitly contain the PFP stress. The PFP stress  $\Sigma_{\text{pfp}}$  is contained in the force density  $n_p \bar{\mathbf{f}}_{\text{pf}}$  as [28,29]

$$n_p(\mathbf{x}) \bar{\mathbf{f}}_{\text{pf}}(\mathbf{x}) = n_p(\mathbf{x}) \mathbf{f}_{\text{pm}}(\mathbf{x}) + \nabla \cdot \Sigma_{\text{pfp}}(\mathbf{x}) + O\left(\frac{\ell_p}{L}\right)^2, \quad (5)$$

where  $\mathbf{f}_{\text{pm}}$  is the particle–mean-field interaction force,  $\ell_p$  is the typical distance among the particles, and  $L$  is the length scale of the physical problem, or the length scale associated with the gradient of the macroscopic field. The PFP stress affects both phases with opposite signs.

Although higher-order terms in  $\ell_p/L$  have been studied for Stokes flows [29], in the present work we only study the first two terms in (5) and limit ourselves to disperse multiphase flows with  $\ell_p \ll L$ . Similarly to the kinetic theory [34,35] for collisional particle-laden flows, the model developed here is not valid for flows with strong spatial gradients, inside a shock wave for instance.

In the following we describe and define the particle–mean-field force  $\mathbf{f}_{\text{pm}}$  and the PFP stress. In general, the phase interaction force (3) is a function of time  $t$ . However, in this work of calculating the force and the PFP stress, we mainly concern about the spatial effects. For brevity, we drop variable  $t$  for time in the rest of the paper. The concepts of the particle–mean-field force  $\mathbf{f}_{\text{pm}}$  and the PFP stress  $\Sigma_{\text{pfp}}$  are valid for time dependent flows, while the numerical results in the following sections are obtained from steady uniform flows.

### B. Nearest particle statistics

To study PFP interactions, we inevitably encounter the difficulty of the long-range hydrodynamic interactions among the particles. To avoid the mathematical difficulties associated with the long-range interactions, which often lead to divergent integrals, we use the nearest particle statistics [28,29]. We divide the ensemble average process into two steps. In the first step, for a particle centered at  $\mathbf{x}$ , we specify a position  $\mathbf{y}$  and surround it with an infinitesimal volume  $d^3y$ , then average over all the configurations in which the volume  $d^3y$  contains centers of the nearest particles to obtain the conditional average  $\bar{\mathbf{f}}_{\text{pf}}^{\text{nst}}(\mathbf{x}, \mathbf{y})$  of the forces  $\mathbf{f}_{\text{pf}}(\mathbf{x}; \mathcal{C})$  acting on the particle at  $\mathbf{x}$  in these configurations. Clearly, there is at least one nearest particle for every particle in a configuration. It is possible that in some configurations the particle at  $\mathbf{x}$  may have two or more, say,  $N_x$ , nearest particles. For such configurations, their contribution to the average is reduced [28,29] by a factor  $1/N_x$ . The dependence of such conditionally averaged force  $\bar{\mathbf{f}}_{\text{pf}}^{\text{nst}}(\mathbf{x}, \mathbf{y})$  on  $\mathbf{y}$  contains information about particle interactions in the mean field consisting of the surrounding fluid and the particles. There is no need (actually, impossible in most cases) to separate the effects from the interaction with the nearest particle and the effects from the interactions with other surrounding particles or the fluid. The multiparticle effects are inseparably included in the conditionally averaged force  $\bar{\mathbf{f}}_{\text{pf}}^{\text{nst}}(\mathbf{x}, \mathbf{y})$ . By studying the dependence of this conditionally averaged force on the nearest particle location, one can explicitly consider the effect of the nearest particle, while the effects from other particles and the surrounding fluid are implicitly included in the conditionally averaged force. The ensemble average of the force is then calculated in the second step as the expected value of these conditionally averaged forces,

$$\bar{\mathbf{f}}_{\text{pf}}(\mathbf{x}) = \int \bar{\mathbf{f}}_{\text{pf}}^{\text{nst}}(\mathbf{x}, \mathbf{y}) P_{\text{nst}}(\mathbf{y}|\mathbf{x}) d^3y, \quad (6)$$

where  $P_{\text{nst}}(\mathbf{y}|\mathbf{x})$  is the probability density of  $\mathbf{y}$  being occupied by the center of the nearest particle to the particle centered at  $\mathbf{x}$ . This probability contains information about particle distribution around  $\mathbf{x}$ . Although, the integration in (6) is over the entire space, the integral converges absolutely because of the rapid far-field decay of the probability density  $P_{\text{nst}}(\mathbf{y}|\mathbf{x})$ . The rigorous mathematical derivation of this relation can be found in recent works [28,29].

The conditional average force  $\bar{\mathbf{f}}_{\text{pf}}^{\text{nst}}(\mathbf{x}, \mathbf{y})$  contains information of the interaction between the nearest particles with the presence of other particles and the fluid. In principle, one can study the average force conditional on the second-, third-, and so on, nearest particles to study physics of multiparticle interactions. This direction is not pursued in this work for two reasons. The first reason is that this approach is similar to the BBGKY hierarchy [36] in kinetic theories, which has only limited success in the study of particle suspensions. Although the mathematical difficulty of divergent integrals for long-range particle interactions is avoided using the nearest particle statistics, the complexity of multiparticle interactions, especially for nonlinear cases, is still formidable. The other more important reason is that, for the purpose of calculating the average force  $\bar{\mathbf{f}}_{\text{pf}}$ , the effects of multiparticle interactions are already included in the conditionally averaged force  $\bar{\mathbf{f}}_{\text{pf}}^{\text{nst}}(\mathbf{x}, \mathbf{y})$ , because it is calculated by averaging over the forces with the presence of all particles.

In kinetic theories [9,30,37], the pair distribution function  $P_2(\mathbf{x}, \mathbf{y})$  is defined such that for differential volumes  $d^3x$  and  $d^3y$  surrounding  $\mathbf{x}$  and  $\mathbf{y}$  respectively,  $P_2(\mathbf{x}, \mathbf{y})d^3x d^3y$  is the probable number of particle pairs with one particle center in  $d^3x$  and the other in  $d^3y$ . The number density

$P(\mathbf{y}|\mathbf{x})$  of having particles at  $\mathbf{y}$  conditional on a particle at  $\mathbf{x}$  can be calculated from the pair distribution function as  $P(\mathbf{y}|\mathbf{x}) = P_2(\mathbf{x}, \mathbf{y})/n_p(\mathbf{x})$ , where  $n_p(\mathbf{x})$  is the particle number density at  $\mathbf{x}$ . In this way,  $P(\mathbf{y}|\mathbf{x})d^3y$  is the probable number of particle centers in  $d^3y$  conditional on  $\mathbf{x}$  being occupied by a particle center. These particles are not necessarily the nearest to the particle at  $\mathbf{x}$ . We use  $\bar{h}_2(\mathbf{x}, \mathbf{y})$  to denote the probability that the particle at  $\mathbf{y}$  is the nearest to the particle at  $\mathbf{x}$  conditional on  $\mathbf{x}$  and  $\mathbf{y}$  being occupied by a pair of particle centers. We can then write

$$P_{\text{nst}}(\mathbf{y}|\mathbf{x}) = \bar{h}_2(\mathbf{x}, \mathbf{y})P(\mathbf{y}|\mathbf{x}) = \bar{h}_2(\mathbf{x}, \mathbf{y})P_2(\mathbf{x}, \mathbf{y})/n_p(\mathbf{x}). \quad (7)$$

Using this relation, we can rewrite (6) as

$$n_p(\mathbf{x})\bar{f}_{\text{pf}}(\mathbf{x}) = \int f_{\text{eb}}(\mathbf{x}, \mathbf{y})P_2(\mathbf{x}, \mathbf{y})d^3y, \quad (8)$$

where

$$f_{\text{eb}}(\mathbf{x}, \mathbf{y}) = \bar{f}_{\text{pf}}^{\text{nst}}(\mathbf{x}, \mathbf{y})\bar{h}_2(\mathbf{x}, \mathbf{y}), \quad (9)$$

is the effective short-range interaction force because of the rapid far-field decay of  $\bar{h}_2(\mathbf{x}, \mathbf{y})$  [28,38,39] and can be regarded as the force on the particle at  $\mathbf{x}$  from the particle at  $\mathbf{y}$  through the effective field consisting of the fluid and the surrounding particles.

### C. The PFP stress and the force decomposition

Comparing this effective short-range force  $f_{\text{eb}}$  with the particle interaction forces in molecular dynamics, this force contains not only PFP interactions but also the particle-fluid interactions. Since the potential part of the virial stress in molecular systems represents interactions among the particles, and its definition requires the interaction forces on a pair of particles be antisymmetric [30] (Newton's third law), we decompose  $f_{\text{eb}}$  into the symmetric part  $f_s$  and the antisymmetric part  $f_a$ . They are

$$f_s(\mathbf{x}, \mathbf{r}) = \frac{1}{2} \left[ f_{\text{eb}}\left(\mathbf{x} - \frac{\mathbf{r}}{2}, \mathbf{x} + \frac{\mathbf{r}}{2}\right) + f_{\text{eb}}\left(\mathbf{x} + \frac{\mathbf{r}}{2}, \mathbf{x} - \frac{\mathbf{r}}{2}\right) \right], \quad (10)$$

and

$$f_a(\mathbf{x}, \mathbf{r}) = \frac{1}{2} \left[ f_{\text{eb}}\left(\mathbf{x} - \frac{\mathbf{r}}{2}, \mathbf{x} + \frac{\mathbf{r}}{2}\right) - f_{\text{eb}}\left(\mathbf{x} + \frac{\mathbf{r}}{2}, \mathbf{x} - \frac{\mathbf{r}}{2}\right) \right]. \quad (11)$$

If we extend Newton's third law and consider the PFP interaction force on a particle in the pair as the component that changes its sign when the particle positions are exchanged, then the antisymmetric  $f_a$  defined in (11) is the force. This force can then be used [28,29] (also shown in the Appendix) to define the PFP stress

$$\begin{aligned} \Sigma_{\text{pfp}}(\mathbf{x}) &= \frac{1}{2} \int \mathbf{r} f_a(\mathbf{x}, \mathbf{r}) P_2\left(\mathbf{x} - \frac{\mathbf{r}}{2}, \mathbf{x} + \frac{\mathbf{r}}{2}\right) d^3r \\ &= \frac{n_p(\mathbf{x})}{2} \int \mathbf{r} \bar{f}_{\text{pf}}^{\text{nst}}(\mathbf{x}, \mathbf{x} + \mathbf{r}) P_{\text{nst}}(\mathbf{x} + \mathbf{r}|\mathbf{x}) d^3r + O(\ell_p/L), \end{aligned} \quad (12)$$

similar to the potential part of the virial stress in molecular dynamics. The second identity of (12) is obtained using (7) and (9).

Meanwhile, the position exchange should not affect the particle-mean-field interaction force; therefore, the symmetric force  $f_s$  defined in (10) is the particle-mean-field force per particle. By integrating over all possible pairs,

$$n_p(\mathbf{x})f_{\text{pm}}(\mathbf{x}) = \int f_s(\mathbf{x}, \mathbf{r}) P_2\left(\mathbf{x} - \frac{\mathbf{r}}{2}, \mathbf{x} + \frac{\mathbf{r}}{2}\right) d^3r, \quad (13)$$

is the averaged particle–mean-field force density. Since  $f_{\text{eb}}$  is a short-range force, so are the forces  $f_s$  and  $f_a$  defined in (10) and (11). The integrations in (12) and (13) are then guaranteed to converge.

The PFP stress introduced here is different from many stresses introduced for the mixture [8] or using kinetic theories [9,10,40], because it presents in both the average momentum equations for the fluid and the particle phases when (5) is used in (1) and (2). The force decomposition is not unique. For instance, the Stokes drag can also be decomposed into this form using the linearity of the Stokes flow [12]. The decomposition introduced here has the advantage of its simple physical meanings for  $f_{\text{pm}}$  and  $\Sigma_{\text{pfp}}$  as described above and is valid for general disperse multiphase flows without limitations on volume fractions or Reynolds numbers.

In cases of statistically homogeneous flows, as in the most numerical simulations performed today [7,21–27,41,42], after taking the divergence in (5), the PFP stress term does not contribute to the phase interaction force  $\bar{f}_{\text{pf}}$ , and therefore, is not studied. The models developed from these works are then for  $f_{\text{pm}}$  only. With the concept of the PFP stress, we can further interrogate the numerical results to obtain the stress. The force decomposition (5) also implies that models for these two closure quantities can be developed individually. Although one can choose to develop a model for the phase interaction force  $\bar{f}_{\text{pf}}$  directly to include the effects of gradients, such as  $\nabla\theta_p$ , the PFP stress represents the unique physics of particle interactions mediated by the fluid at the scale of mean particle distance.

When the averaged equations (1) and (2) are applied to a problem, it is often assumed that the interparticle length scale  $\ell_p$  is much smaller than the length scale  $L$  of the physical problem ( $\ell_p \ll L$ ). Since  $\mathbf{r}$  is of order  $\ell_p$ , the PFP stress is of order  $\ell_p n_p \bar{f}_{\text{pf}}^{\text{nst}}$ . Relation (5) shows the effect of the PFP stress is of order  $\ell_p/L$  as the divergence operator  $\nabla$  in (5) is of order  $1/L$ . To be correct to this order in the momentum equations, the effect of gradients of the mean fields on the PFP stress can be neglected. The PFP stress models developed in statistical homogeneous systems are then valid to statistically inhomogeneous systems, if an error higher than the first order of  $\ell_p/L$  is tolerated. However, this does not imply that the statistical inhomogeneity has no effect on the force  $f_{\text{pm}}$ . The examples include the lift force and the convective derivative terms in the added mass force.

In the following sections, we calculate the PFP stress in statistically steady, homogeneous flows through arrays of randomly distributed equal-size spheres. These are clearly idealized cases. Most disperse multiphase flows contain mesoscale structures [14,15,41], and particle distributions are not random and homogeneous. We limit ourselves to study these idealized cases for three reasons. First, the PFP stress is a new concept. To understand its properties we choose to start with simple systems. Second, the PFP stress calculated from a uniform system is applicable in models correct to the first order of  $\ell_p/L$  as mentioned above. Third, most simulations performed today are limited to the uniform systems. For Stokes flows, simple shear motions have been simulated [41]. For cases with more general velocity gradients, the deformation of the computational domain, which are often periodic, has to be considered to accommodate particle motions. Although, a recent technique [43,44] allows for simulations of uniform velocity gradients with full matrices in a periodic domain, the effect of particle volume fraction gradient can still not be considered using periodic domains.

### III. NUMERICAL SIMULATIONS

Since the calculation of forces on moving particles requires tracking particle-fluid interfaces and is more difficult, in the work we only study the PFP stress in flows with stationary particles. We assume that the closure for the PFP stress exists, that is it can be expressed as a function of the macroscopic quantities. Without a spatial gradient, the stress can only depend on the particle volume fraction  $\theta_p$ , relative velocity  $\mathbf{v}_p - \mathbf{v}_f$  between the phases, viscosity  $\mu_f$ , density  $\rho_f$  of the fluid, and the particle size  $d_p$ . The only tensor with the dimension of stress can be constructed from these variables is of form

$$\Sigma_{\text{pfp}} = \rho_f \theta_p [B_1(\theta_p, \text{Re})(\mathbf{v}_p - \mathbf{v}_f) \cdot (\mathbf{v}_p - \mathbf{v}_f) \mathbf{I} + B_2(\theta_p, \text{Re})(\mathbf{v}_p - \mathbf{v}_f)(\mathbf{v}_p - \mathbf{v}_f)], \quad (14)$$

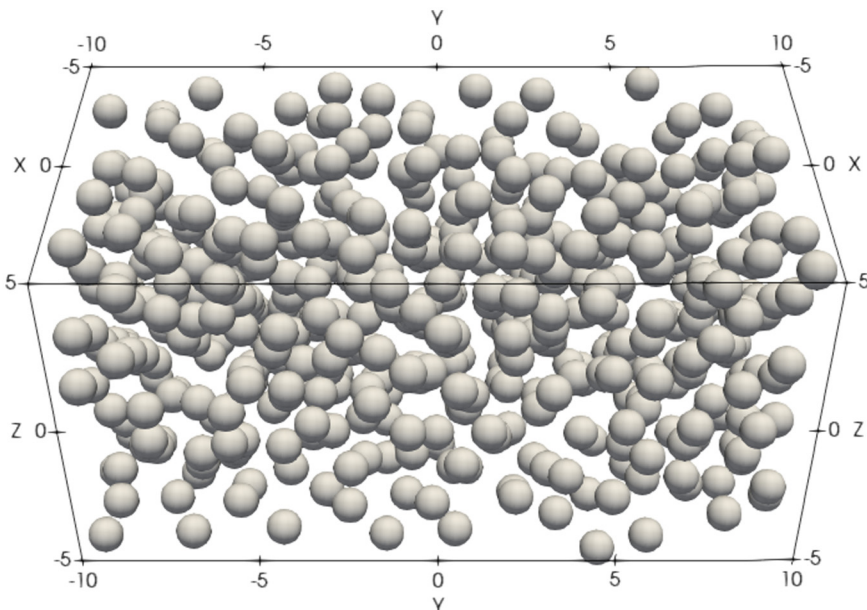


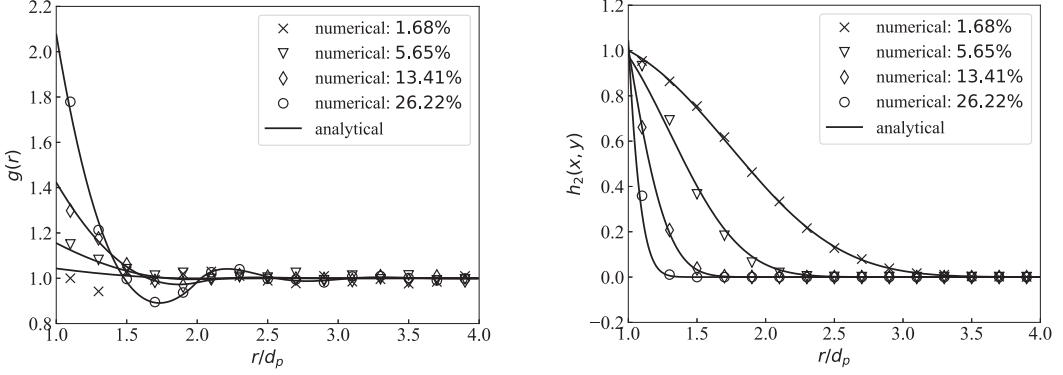
FIG. 1. Sample packing with volume fraction 13.41%.

where  $B_1$  and  $B_2$  are dimensionless coefficients that depend on the particle volume fraction  $\theta_p$  and the particle Reynolds number  $\text{Re} = \rho_f |\mathbf{v}_p - \mathbf{v}_f| d_p / \mu_f$ . For systems with moving particles, the coefficients can also be functions of density ratio between the phases. These coefficients are calculated in Sec. IV.

#### A. Configuration setup and particle statistics

The numerical simulation is performed in a cuboid domain containing fixed spherical particles as illustrated in Fig. 1. Periodic boundary conditions are applied in the  $x$  and  $z$  directions, and the flow is in the  $y$  direction. For a specified particle volume fraction  $\theta_p$ , we first place spherical particles of diameter  $d_p$  according to the face-centered cubic lattice in a cuboid. The lattice size of each cube is given as  $\ell = \sqrt[3]{(\pi/3\theta_p)} d_p$ , to ensure the particle volume  $\theta_p$ . The maximum particle volume fraction can be accommodated is  $\sqrt{3}\pi/8 \approx 0.68$  without overlap. To generate random particle distribution, each particle is subjected to 10 000 random displacements with the maximum magnitude equals to a fraction (0.05) of the mean gap  $\sqrt{3}\ell/2 - d_p$  between the particles. If a displacement causes particles to overlap, then the displacement is discarded, and the particle remains in the original place. Particles close to a periodic boundary are checked for overlap with the images of the particles near the opposite boundary. When a particle moves out of the domain, it comes in from the opposite side of the boundary. In this way, the total particle number remains constant during each random displacement. Figure 1 shows a random particle distribution generated using this method with the particle volume fraction 13.41%. The length in the figure is nondimensionalized by the particle diameter.

For homogeneous and isotropic particle distributions, both the nearest particle probability  $\bar{h}_2(\mathbf{x}, \mathbf{y})$  and the pair distribution function  $P_2(\mathbf{x}, \mathbf{y})$  are only functions of particle separation  $r = |\mathbf{y} - \mathbf{x}|$ . We then write  $\bar{h}_2(\mathbf{x}, \mathbf{y}) = \bar{h}_2(r)$  and  $P_2(\mathbf{x}, \mathbf{y}) = n_p^2 g(r)$ , where  $g(r)$  is the radial distribution function. The probability density  $P(\mathbf{y}|\mathbf{x})$  of finding a particle at  $\mathbf{y}$  conditional on a particle at  $\mathbf{x}$  is  $P(\mathbf{y}|\mathbf{x}) = P_2(\mathbf{x}, \mathbf{y})/n_p = n_p g(r)$ . The probability density of finding the nearest particle at  $\mathbf{y}$  knowing a particle already at  $\mathbf{x}$  becomes  $P_{\text{nst}}(\mathbf{y}|\mathbf{x}) = n_p g(r) \bar{h}_2(r)$ . For a random distribution of equal-size


 FIG. 2. Comparison of radial distribution function  $g(r)$  and probability  $\bar{h}_2(\mathbf{x}, \mathbf{y})$ .

spheres with diameter  $d_p$ , Torquato *et al.* [38,39] calculated the nearest-neighbor distribution function  $H(r)$  defined such that for an infinitesimal  $dr$  and a given sphere,  $H(r)dr$  is the probability of finding its nearest neighbor in the distances between  $r$  and  $r + dr$ . In the case of isotropic and homogeneous suspension of spheres, this function is related to the probability of nearest particle  $\bar{h}_2$  as  $H(r) = 4\pi r^2 P_{\text{nst}}(\mathbf{y}|\mathbf{x}) = 4\pi r^2 n_p g(r) \bar{h}_2(r)$ .

For hard spheres Torquato *et al.* [38,39] found the analytical solution for function  $H(r)$ ,

$$H(r) = \frac{24\theta_p}{d_p} (C_e x^2 + C_f x + C_g) \exp\{-\theta_p [8C_e(x^3 - 1) + 12C_f(x^2 - 1) + 24C_g(x - 1)]\}, \quad (15)$$

where

$$x = \frac{r}{d_p}, \quad C_e = \frac{1 + \theta_p}{(1 - \theta_p)^3}, \quad C_f = -\frac{\theta_p(3 + \theta_p)}{2(1 - \theta_p)^3}, \quad \text{and} \quad C_g = \frac{\theta_p^2}{2(1 - \theta_p)^3}. \quad (16)$$

Using this solution, and the solution [45] for the radial distribution function  $g(r)$ , we can calculate  $h_2(r)$  analytically. To assess the quality of the random particle assemblies generated above, we numerically calculate the radial distribution function  $g(r)$  and the nearest particle probability  $h_2(r)$  to compare with the analytical results in Fig. 2.

To obtain numerical results of the radial distribution function  $g(r)$  and probability  $\bar{h}_2(\mathbf{x}, \mathbf{y})$  in the figure, we generated  $N_{\text{en}} = 200, 30, 10,$  and  $5$  configurations for particle volume fractions 1.68%, 5.65%, 13.41%, and 26.22%, with  $N_p = 64, 216, 512,$  and  $1000$  equal-size particles respectively. We then surround every particle with 20 layers of spherical shells of thickness  $\Delta r = d_p/5$ , and then loop through all the particles in all configurations and count the number  $N_i$ , ( $i = 1, 2, \dots, 20$ ), of particles in the shells and the numbers  $N_{\text{nst},i}$  of the nearest particles in the shells. The numerical results of the probability  $\bar{h}_2(r)$  and radial distribution function  $g(r)$  are calculated as

$$\bar{h}_2(r_i) = \frac{N_{\text{nst},i}}{N_i}, \quad g(r_i) = \frac{N_i}{4\pi r_i^2 n_p \Delta r N_{\text{en}} N_p}, \quad (17)$$

with  $r_i = d_p + (i - 1/2)\Delta r$ .

## B. The numerical solution method

With the particle configurations generated by the method described above, particle-resolved simulations are carried out. The Navier-Stokes equation is solved using a high-order fluid solver NEK5000 based on the spectral element method [46]. In this work, the Gauss-Lobatto-Legendre points using fifth-order polynomials are adopted for velocity interpolation, with six interpolants in each direction. For the pressure calculation, the third-order Gauss-Lobatto-Legendre points are



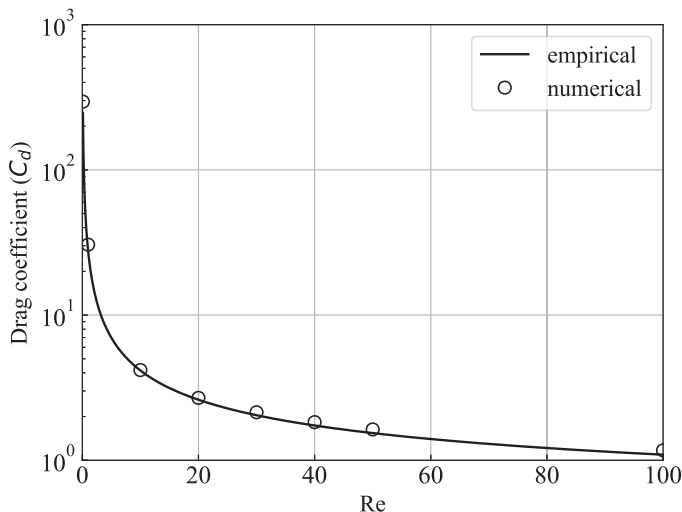


FIG. 3. Comparison of drag coefficients for a single sphere with different Reynolds numbers.

employed. Since the main objective of this work is to calculate the new PFP stress, in this section we focus on the validation of the numerical method with the calculations of the drag force for a single sphere and the average drag force in disperse multiphase flows with different volume fractions and Reynolds numbers. Readers interested in the details of the numerical method and the code (NEKIBM) are referred to the recent publication [47].

To validate the numerical tool (NEKIBM) used in this work, the flow past a sphere is first simulated and compared with the empirical relation [48]. In this benchmark calculation, the length is nondimensionalized by the sphere diameter  $d_p$ . The fluid domain is  $10 \times 20 \times 10$  and divided into  $40 \times 80 \times 40$  spectral elements in  $x, y, z$  directions, implying four cells across a particle diameter or  $\Delta x = \Delta y = \Delta z = d_p/4$ . The origin of coordinate system is selected as the center of the domain. A solid sphere is fixed at position  $(0, -1, 0)$ . The time step used in the calculation is  $dt = 10^{-3} \text{Re} d_p/U$  where  $U$  is the characteristic velocity, and  $\text{Re}$  is the Reynolds number based on the particle diameter. The corresponding convection Courant-Friedrichs-Lewy (CFL) number  $dt U/\Delta x = 4 \times 10^{-3} \text{Re}$ , and the momentum diffusion CFL number  $dt \mu_f/[\rho_f (\Delta x)^2] = 0.016$ , where  $\mu_f$  is the fluid viscosity. The Reynolds number simulated in this calculation of the single sphere drag ranges from 0.1 to 100. The maximum convection CFL number is 0.4. The flow is in the  $y$  direction with the uniform inlet velocity determined by the Reynolds number. At the outlet the convective outflow condition is applied. Periodic boundary conditions are applied to other boundaries. The calculated drag coefficient is plotted in Fig. 3 showing a good comparison with the well-known empirical correlation [48]

$$C_d = \frac{24(1 + 0.15\text{Re}^{0.687})}{\text{Re}}. \quad (18)$$

### C. Drag calculation

The same NEKIBM used in the calculation of single sphere force is used to calculate the hydrodynamic force

$$\mathbf{f}_h(\mathbf{x}, \mathcal{C}) = \oint \boldsymbol{\sigma}_s(\mathbf{z}, \mathcal{C}) \cdot \mathbf{n} dS, \quad (19)$$

on a particle in the configurations generated as described above. This force from NEKIBM corresponds to the first term inside the square bracket in (3), and the effect of the average fluid stress  $\boldsymbol{\sigma}_f$  has not been subtracted off. In a uniform and isotropic distribution of stationary rigid particles with a uniform average fluid velocity field, the average of the strain rate of the fluid is zero [32], and so is the average viscous stress. The average fluid stress becomes  $\boldsymbol{\sigma}_f = -p_f \mathbf{I}$ , where  $p_f$  is the average fluid pressure and  $\mathbf{I}$  is the identity tensor. The force (19) calculated from the NEKIBM method includes contribution from the pressure gradient force. In flows such as those simulated in this work and by Tenneti *et al.* [42], a pressure gradient is used to drive the relative motions between the particle and the fluid, while in other cases, such as those with the presence of gravity, the buoyancy force exists even without a relative motion between the phases. For the convenience of model development, it is advantageous [31,32,49] to separate the effect of the buoyancy-like term from the effect of relative motion between the phases, which is generally called the drag force in a steady and uniform flow. Using  $\boldsymbol{\sigma}_f = -p_f \mathbf{I}$  in (3), one can write

$$\mathbf{f}_{\text{pf}}(\mathbf{x}, t; \mathcal{C}) = \mathbf{f}_h + V_p \nabla p_f, \quad (20)$$

where  $V_p$  is the particle volume. For the uniform particle distribution and average fluid velocities simulated in this work and by Tenneti *et al.* [42], using the momentum equation (1) and (20), one finds the balance between the gradient of the average pressure and the average hydrodynamic force on particles,

$$-\nabla p_f = n_p \bar{\mathbf{f}}_h \quad \text{and} \quad \bar{\mathbf{f}}_{\text{pf}} = (1 - \theta_p) \bar{\mathbf{f}}_h. \quad (21)$$

Considering the effects of particle volume fraction and Reynolds number, for the monodisperse systems an empirical relation for the average hydrodynamic force has been written [42] as

$$\bar{\mathbf{f}}_h = 3\pi \mu_f d_p (1 - \theta_p) (\mathbf{v}_p - \mathbf{v}_f) F_d(\theta_p, \text{Re}_m), \quad (22)$$

where

$$F_d(\theta_p, \text{Re}_m) = \frac{1 + 0.15 \text{Re}_m^{0.687}}{(1 - \theta_p)^3} + F_{\theta_p} + F_{\theta_p, \text{Re}_m}, \quad \text{Re}_m = \frac{\rho_f |\mathbf{v}_p - \mathbf{v}_f| d_p (1 - \theta_p)}{\mu_f}, \quad (23)$$

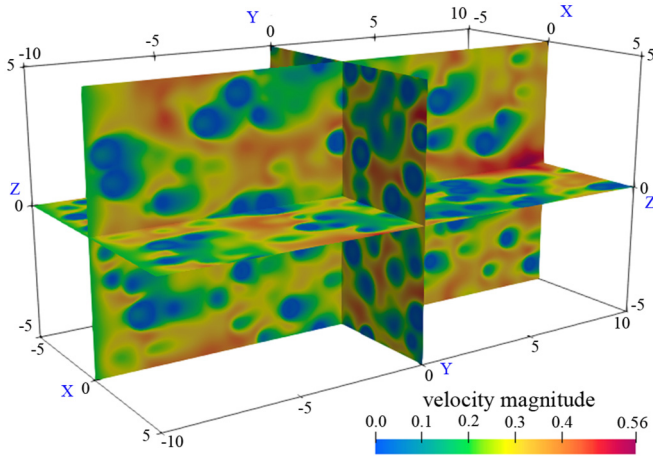
$$F_{\theta_p} = \frac{5.81 \theta_p}{(1 - \theta_p)^3} + \frac{0.48 \theta_p^{1/3}}{(1 - \theta_p)^4}, \quad F_{\theta_p, \text{Re}_m} = \theta_p^3 \text{Re}_m \left[ 0.95 + \frac{0.61 \theta_p^3}{(1 - \theta_p)^2} \right]. \quad (24)$$

Since  $3\pi \mu_f d_p (\mathbf{v}_p - \mathbf{v}_f)$  in (22) is the Stokes drag of a single sphere, the function  $F_d(\theta_p, \text{Re}_m)$  is called the normalized drag. We note that this normalized drag is written in terms of the mean Reynolds number  $\text{Re}_m$  defined in (23), which is different from the particle Reynolds number  $\text{Re}$  by a factor  $(1 - \theta_p)$ .

To calculate the PFP stress, simulations with four mean Reynolds numbers  $\text{Re}_m = 10, 20, 60,$  and  $100$  are carried out for four particle volume fractions  $\theta_p = 1.68\%, 5.65\%, 13.41\%,$  and  $26.22\%$ . Flows are in the  $y$  direction coming from the left as illustrated in Fig. 1 with a prescribed uniform velocity on the left surface. Figure 4 shows one of the calculated flow fields.

Since the left and right boundaries are not periodic boundaries, there are leading and trailing edge effects. To assess them, we divide the computational domain into 20 segments along the flow direction, and plot the average normalized drag  $F_d(\theta_p, \text{Re}_m)$  for particles with their centers in the segments. The results are shown in Fig. 5. The figure shows that the average particle force, and hence average flow field can be considered as statistically homogeneous from segments 5 to 17. The forces from these segments are then used in our statistical analysis in the reminding of this work.

Figure 6 shows comparison of the normalized drag obtained from NEKIBM calculations to the empirical relation (23). Reasonable agreements are found between these NEKIBM results and those from the finite difference method [42], further validating the particle force calculation in this work.


 FIG. 4. Fluid velocity contour in a flow with  $Re_m = 20$  and  $\theta_p = 13.41\%$ .

#### IV. NUMERICAL RESULTS

##### A. The antisymmetric force

Since the PFP stress is caused by the antisymmetric force  $f_a$  on a particle, we now study its property in the homogeneous flows simulated in this work. The flow is along the  $y$  direction. With randomly distributed particles, for a particle with its nearest neighbor at distance  $r$  away, the effective short-range force  $f_{eb}$ , and hence  $f_a$ , is on the plane formed by vector  $r$  and the  $y$  axis, because of the symmetry about the plane. We can then decompose the force  $f_a$  into a component  $f_{\parallel}$  parallel to the flow along the  $y$  axis and a component  $f_{\perp}$  perpendicular to the flow as shown in Fig. 7.

These force components are functions of  $r$  and  $\theta$  only and is independent of  $\varphi$  because of the axis symmetry about the  $y$  axis. We study these force components for two intervals of the  $\theta$  values

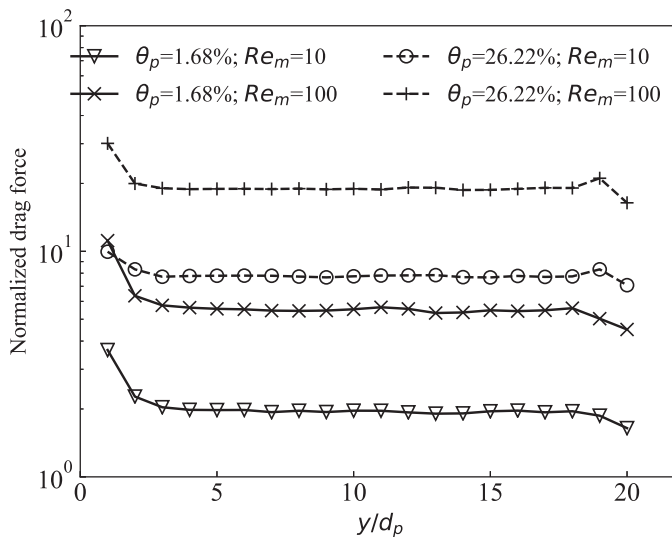


FIG. 5. Variation of normalized drag along flow direction

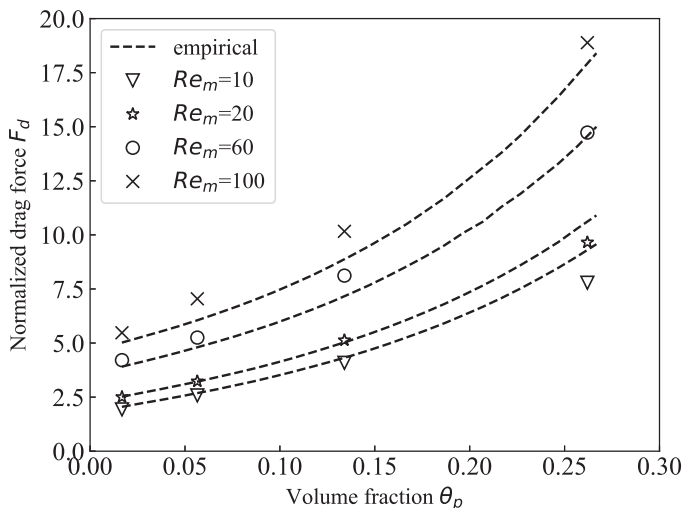


FIG. 6. Comparison of numerically calculated normalized drag with the empirical relation [42] (23).

in our simulated flows with  $Re = 20$  and particle volume fraction  $\theta_p = 5.65\%$ . The first interval is  $85^\circ < \theta < 95^\circ$ . The nearest pairs are almost perpendicular to the flow. In this interval, the average of the force components  $f_{\parallel}$  vanishes. Figure 8 shows average  $f_{\perp}$  normalized by the mean drag  $f_{pm}$  as a function of  $r$ , the distance between the nearest particles. The value of this force is negative, in the direction opposite to  $r$ , implying repulsion between the particles. This repulsion is caused by flow diversion around the nearest particle. According to Seyed-Ahmida and Wachs [50] (in their Fig. 5), the maximum  $|f_{\perp}|$  does not happen at  $\theta = 90^\circ$ , but at an angle somewhat downstream, where the flow diversion by the nearest particle is the strongest. This repulsion results in the negative PFP stress in the direction perpendicular to the flow as calculated below.

Another interval of  $\theta$  studied is  $-10^\circ < \theta < 10^\circ$ . Within this  $\theta$  interval the nearest neighbors of the particles are almost directly down stream of the particle. The average perpendicular component  $f_{\perp}$  is zero. Figure 8 also shows the average parallel components  $f_{\parallel}$  normalized by the mean drag  $f_{pm}$  as a function of  $r$ . The plotted values are not smooth, because in the simulated flows, we only find less than 10 nearest pairs in this  $\theta$  interval for the two values between 1.5 and 2.0 of  $r/d_p$  in the figure. The value of this function is positive, which confirms the fact that the leading particle (with positive  $r$ ) is subjected to a greater force compared to mean force on the pair. Since  $f_a$  is antisymmetric, if the  $\theta$  interval is changed to  $170^\circ < \theta < 190^\circ$ , then the force component  $f_{\parallel}$  changes its sign and becoming negative, which implies trailing particle is subjected to less force than

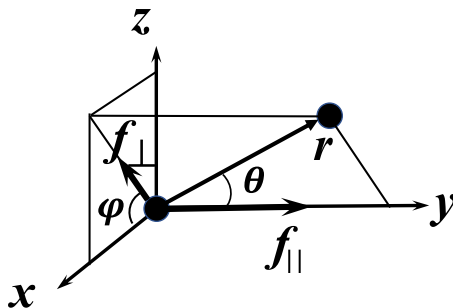


FIG. 7. Decomposition of the antisymmetric force  $f_a$ .

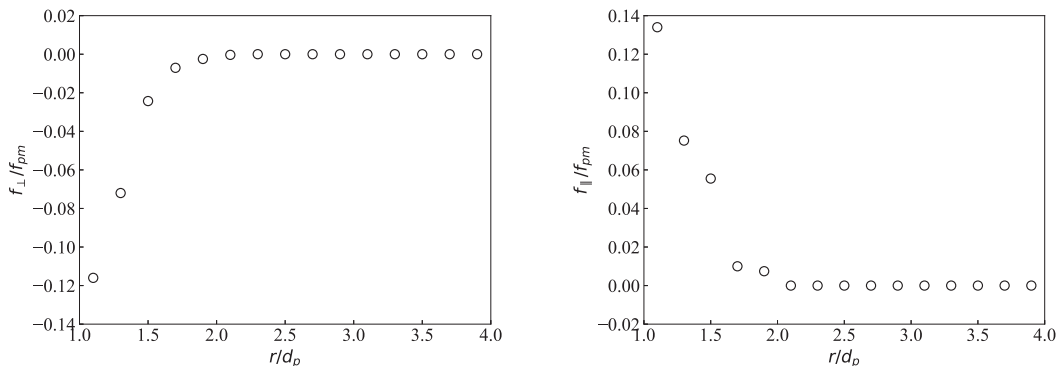


FIG. 8. Normalized  $f_a$  when the nearest pairs are almost perpendicular (left) and parallel (right) to the flow.

the mean. This observation is also consistent with the calculation by Seyed-Ahmida and Wachs [50]. These properties of the forces on the leading and trailing particles imply attraction between the particles in direction parallel to the flow and the positive PFP stress as calculated below.

### B. The PFP stress

After exploring the properties of the probability density and the related forces of the nearest particles in the homogeneous and isotropic particle distributions and verifying our particle force calculation in the previous section, we now calculate the PFP stress. In an isotropic system, there is no preferred direction. We then have  $\int \mathbf{r} P_{\text{nst}}(\mathbf{r} + \mathbf{x}|\mathbf{x}) d^3 r = \mathbf{0}$ . Using this relation and noting that  $\nabla p_f$  is independent of  $\mathbf{r}$ , we use (20) to rewrite the PFP stress defined in (the second line of) (12) as

$$\Sigma_{\text{pfp}} = \frac{n_p}{2} \int \mathbf{r} \overline{\mathbf{f}_h^{\text{nst}}} P_{\text{nst}}(\mathbf{r} + \mathbf{x}|\mathbf{x}) d^3 r. \quad (25)$$

With this relation, we note that in obtaining (6), the force on the particle is used as an example. The same procedure described in Sec. II can be used to show that relation (6) is valid for any particle quantity of interest [28,29]. We now set the particle quantity to be  $\mathbf{r} \mathbf{f}_h$ , where  $\mathbf{f}_h$  is the hydrodynamic force (19) on a particle, and  $\mathbf{r}$  is the distance from the particle to its nearest neighbor. If the particle has multiple nearest particles (a zero probability event and not encountered in the simulations performed in this work), then this distance is the average of the distances to the nearest particles. In this way, quantity  $\mathbf{r} \mathbf{f}_h$  is a well-defined quantity for each particle. Using (6) on this quantity (replacing  $\overline{\mathbf{f}_{\text{pf}}}$  by  $\mathbf{r} \mathbf{f}_h$ ), and noting  $\overline{(\mathbf{r} \mathbf{f}_h)^{\text{nst}}} = \overline{\mathbf{r} \mathbf{f}_h^{\text{nst}}}$ , we find the integral in (25) is the ensemble average  $\overline{\mathbf{r} \mathbf{f}_h}(\mathbf{x})$  of the particle quantity at location  $\mathbf{x}$ . In cases of uniform flows, this quantity is independent of  $\mathbf{x}$  and can be calculated as the volume average over the domain, which is segments 5 to 17 described above. Let  $N_t$  be the total number of the particles in the averaging domain. The volume average of  $\mathbf{r} \mathbf{f}_h$  can be calculated as  $\sum_{i=1}^{N_t} \mathbf{r}_i \mathbf{f}_{h,i} / N_t$ , where  $\mathbf{f}_{h,i}$  is the hydrodynamic force on particle  $i$  in the domain, and  $\mathbf{r}_i$  is the distance of particle  $i$  to its nearest neighbor. The PFP stress from (25) then becomes

$$\Sigma_{\text{pfp}} = \frac{n_p}{2N_t} \sum_{i=1}^{N_t} \mathbf{r}_i \mathbf{f}_{h,i}. \quad (26)$$

This expression is similar in form to the definition of the virial stress [30,51] in particle systems, but with different meanings for the quantities involved. Here the summation is over all particles in the domain,  $\mathbf{r}_i$  is the distance from particle  $i$  to its nearest neighbor, and  $\mathbf{f}_{h,i}$  is the force on particle  $i$ . In contrast, in the definition for the virial stress, the summation is over all possible particle pairs, not only the nearest one, the distance is between the particles in the pair, and the force is the force

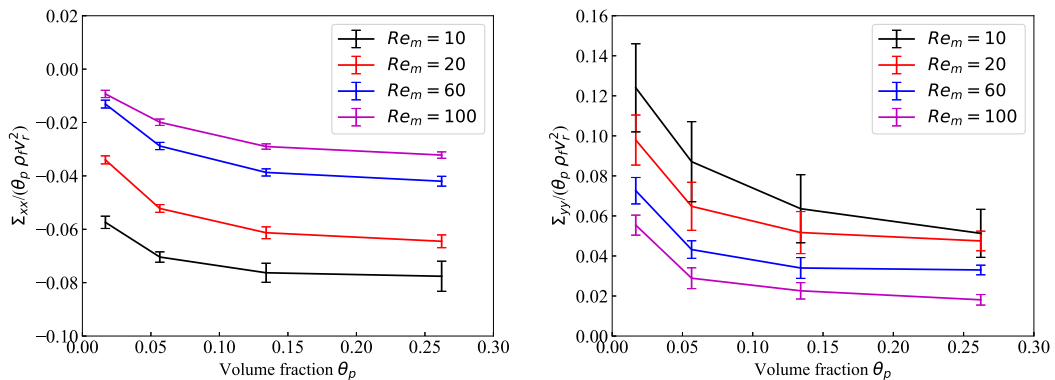


FIG. 9. Normalized  $\Sigma_{xx}$  and  $\Sigma_{yy}$  under different  $\theta_p$  and  $Re_m$ . In the  $y$  labels,  $v_r = |\mathbf{v}_f - \mathbf{v}_p|$  is the magnitude of the relative velocity

contributed by the other particle in the pair, which requires decomposition of the force on a particle into pairwise interactions and is impossible for most cases. Even if such force decomposition is possible for some dilute particle suspensions, for long-range interaction forces, the sum divided by  $N_i$  diverges strongly as the computation domain increases. The stress defined in (26) is guaranteed to converge as the computation domain increases because of the rapid far-field decay of the nearest particle probability, which limits the probability of having large  $r_i$  in the summation.

In our simulations  $N_i$  ranges from about 3250 for the case of particle volume fraction 26.22% to about 8320 for the case of particle volume fraction 1.68%. The PFP stress values reported in Fig. 9 are the averages of the volume averaged stresses from (26) over 10 to 120 particle configurations depending on the particle volume fractions and the Reynolds numbers. More configurations are simulated for small particle volume fractions and small Reynolds numbers, since the PFP stresses fluctuate in larger ranges in these cases. The standard deviations of the stresses over the simulated configurations are also shown in the figures.

Since the flow is in the  $y$  direction, because of the symmetry, the PFP stress takes form  $\Sigma_{\text{pfp}} = \text{diag}[\Sigma_{xx}, \Sigma_{yy}, \Sigma_{zz}]$ , with  $\Sigma_{xx} = \Sigma_{zz}$ . These properties of the stress are confirmed by the numerical results. The calculated off-diagonal elements are at least an order of magnitude smaller than the diagonal elements. The difference between numerically calculated  $\Sigma_{xx}$  and  $\Sigma_{zz}$  is also negligible. Figure 9 shows the normalized  $\Sigma_{xx}$  and  $\Sigma_{yy}$  as functions of the volume fraction  $\theta_p$  at various mean Reynolds number  $Re_m$ .

Using these results, we calculate coefficients  $B_1$  and  $B_2$  in (14) for the PFP stress. The results are plotted in Fig. 10. It appears that these coefficients can be fitted with  $B_1 = 0.95Re^{0.02} - 0.01 \ln(\theta_p) - 1.0915$  and  $B_2 = 0.4046Re^{-0.3} - 0.0412$ , where  $Re = \rho_f v_r d_p / \mu_f$  is the particle Reynolds number. The small exponents of the Reynolds numbers do not imply their weak dependence on the Reynolds number. In the range (from  $Re = 10$  to  $100$ ) simulated in this work, the magnitude of coefficient  $B_1$  decreases by a factor of 2 to 6 depending on the volume fraction, while  $B_2$  decreases by a factor of 4 and appears less dependent on the particle volume fraction. These empirical correlations for the coefficients are only obtained from the simulations within the limited range of the Reynolds numbers. Their extrapolation out of this range should be cautioned. For instance the signs of the correlation change for high Reynolds numbers.

As shown in Fig. 9, in the streamwise direction the stress  $\Sigma_{yy}$  is positive, indicating attraction between particles. In the transversal direction the stress  $\Sigma_{xx} = \Sigma_{zz}$  is negative, indicating repulsion among the particles. Although these results are obtained with stationary particles, which can be considered as the limit of large density ratio between the particle and fluid phases, these properties of the PFP stress are also expected for moving particles. For a group of particles moving in a fluid, the attractive stress in the streamwise direction causes the drafting effect and tends to reduce

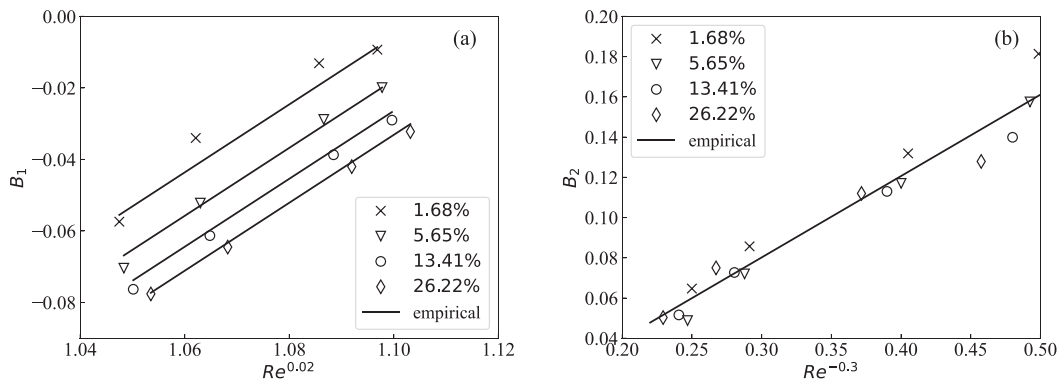


FIG. 10. Coefficients  $B_1$  and  $B_2$  as functions of  $Re$  and  $\theta_p$  (a)  $B_1$  with different  $\theta_p$  (b)  $B_2$  as a function of  $Re$ .

their distances in the direction, while the repulsive stress causes particles to spread out in the directions transversal to the flow. This property of the PFP stress suggests that it is a macroscopic representation of the drafting–kissing–tumbling mechanism [16] in the flow regimes studied here. The trace of the PFP stress is negative in all the results calculated in this work, indicating an overall repelling effect among particles.

The PFP stress involves interaction among particles. One might expect at the limit of small volume fraction  $\theta_p$ , the stress is of  $O(\theta_p^2)$ , since that is the order of the probability of finding a pair of particles around a location. In contrast to this expectation, as shown in Fig. 9 the normalized PFP stress  $\Sigma_{yy}/(\theta_p \rho v_r^2)$  in the streamwise direction increases as the volume fraction  $\theta_p$  decreases, suggesting that the stress could be more important than the first order in the limit of a small particle volume fraction. This is a character of the long-range hydrodynamic interaction of the force moment  $\overline{r f_{pf}^{nst}}$  between the particles. The estimate of  $O(\theta_p^2)$  for particle interactions in the limit of dilute particle phase is only valid for short-range particle interactions [18,28]. Although, the phase interaction force density in momentum equations (1) and (2) caused by the particle drag is only of the first order in the particle volume fraction, the small coefficients  $B_1$  and  $B_2$  in (14) make the drag still the dominating term in the phase interaction force (5) in the direction of relative motion between the phases.

By approximating the particle-mean-field force  $\overline{f_{pm}}$  in (5) as the drag modeled by  $C_d \rho_f (v_p - v_f)^2$  with the drag coefficient  $C_d$ , one can calculate the ratio  $R = d_p B / (C_d L)$  between PFP stress contributions and the drag, where  $B$  is the magnitude of coefficients  $B_1$  and  $B_2$ , and  $L$  is length scale of the flow variation, such as the particle cluster size, or the length associated with the volume fraction gradient. This ratio is typically small. This confirms that in the flow direction the PFP stress can be neglected in the calculation of mean relative velocity between the phases. In the directions perpendicular to the flow, the divergence of the stress is the only force if the velocity field is uniform, hence without the lift force.

As the first calculation of the PFP stress, our numerical results here are limited to fixed particles due to the difficulty of tracking particle motions in the particle resolved simulations. For cases of moving particles, the flow induced anisotropy of particle distribution and history of the wakes of the particles are expected to affect numerical values of the stress, while the qualitative properties of attraction along the flow direction and repulsion in the directions perpendicular to the flow are expected to be valid. If we consider the sedimentation of a particle cloud, then the PFP stress has little direct effect on the sedimentation velocity, but it affects the relative positions among the particles in the cloud and the evolution of the shape of the cloud by attracting particles in the flow direction and repelling them in the perpendicular directions. The timescale of the drag on a particle can be estimated as  $\tau = d_p / [C_d (v_p - v_f)]$ . The timescale associated with the PFP stress is then  $\tau / R = L / [B (v_p - v_f)]$ . For the  $B_1$  and  $B_2$  values calculated above, this timescale implies a

TABLE I. Comparison of coefficients for PFP and Reynolds stresses.

Cases	$D_1$	$D_2$	$B_1$	$B_2$
$\theta_p = 5.65\%$ , $\text{Re}_m = 10$	-0.239	-3.229	-0.070	0.160
$\theta_p = 5.65\%$ , $\text{Re}_m = 60$	-0.195	-3.174	-0.029	0.072
$\theta_p = 13.41\%$ , $\text{Re}_m = 20$	-0.201	-2.009	-0.061	0.113
$\theta_p = 13.41\%$ , $\text{Re}_m = 100$	-0.176	-2.165	-0.027	0.052
$\theta_p = 26.22\%$ , $\text{Re}_m = 20$	-0.143	-1.263	-0.065	0.112
$\theta_p = 26.22\%$ , $\text{Re}_m = 100$	-0.141	-1.462	-0.035	0.063
Dilute potential flow [31,52]	-0.15	-0.05		

significant particle cloud deformation when relative motion between the cloud and the fluid is about 5 to 20 times of the cloud size depending on the Reynolds number and the particle volume fraction. This analysis suggests that the timescale associated with the PFP stress is about the deformation of a particle cloud, while the timescale associated with the drag force is related to the time of the fluid passing a particle. The deformation of the particle cloud then affects the drag and the sedimentation velocity [33]. Furthermore, as calculated below, the PFP stress is of the same order of the fluid Reynolds stress depending on the Reynolds number and the volume fraction.

### C. Reynolds stress

Other than the PFP stress, affecting averaged momentum equation (1), there are two other stresses  $\theta_f \sigma_f^{\text{Re}}$  and  $\theta_p \mathbf{T}_f$ . For potential flows, these stresses take the similar functional form [31,52] as (14). Despite this similarity, there is a significant difference among them. Stresses  $\theta_f \sigma_f^{\text{Re}}$  and  $\theta_p \mathbf{T}_f$  appear only on the averaged momentum equation for the fluid phase, while the PFP stress appears on both averaged momentum equations for the fluid and the particle phases. In cases of dilute particle phase, after dividing (2) by  $\theta_p$ , one finds that the contribution from streamwise PFP stress component to the particle momentum equation is  $\rho_f B_2 v_r^2$  and is of the zeroth order in the particle volume fraction  $\theta_p$ , while this term is multiplied by  $\theta_p$  in the momentum equation (1) for the fluid phase. In this limit, the PFP stress affects the particle motion more than the fluid phase motion.

In our numerical simulations, since the flow field is solved, one can also use the results to calculate the Reynolds stress [53,54]  $\theta_f \sigma_f^{\text{Re}}$ . With the particles fixed, for the same reason as (14), the fluid Reynolds stress can be written as

$$\theta_f \sigma_f^{\text{Re}} = \rho_f \theta_p [D_1(\theta_p, \text{Re})(\mathbf{v}_p - \mathbf{v}_f) \cdot (\mathbf{v}_p - \mathbf{v}_f) \mathbf{I} + D_2(\theta_p, \text{Re})(\mathbf{v}_p - \mathbf{v}_f)(\mathbf{v}_p - \mathbf{v}_f)]. \quad (27)$$

This fluid Reynolds stress  $\sigma_f^{\text{Re}}$  can be calculated with the fluid velocity fluctuations in the homogeneous flow region, segments 5 to 17 in the computational domain. The coefficients  $D_1$  and  $D_2$  in (27) are then calculated. Their values are listed in Table I. In the table, as a comparison, the analytic values of these two coefficients are also listed for dilute particle phase in a potential flow. It is shown that  $D_1$  values from our simulations are about the same order as the one from the dilute potential flow, while the magnitudes of  $D_2$  from the simulations are much greater than the one from the potential flow. This observation can be explained by physics represented by these coefficients in the flow fields around a particle in a potential flow and in a finite Reynolds number flow. The coefficient  $D_1$  represents the isotropic part of the velocity fluctuations, which is the only contribution to the Reynolds stress in the directions perpendicular to the mean flow. These velocity fluctuations are mostly caused by the flow diversion around the particles. The coefficient  $D_2$  represents the velocity fluctuations in the relative mean flow direction. In this direction the potential flow is symmetric in the downstream and the upstream directions, while for a finite Reynolds number flow, the symmetry is broken and the effect of wake is important.



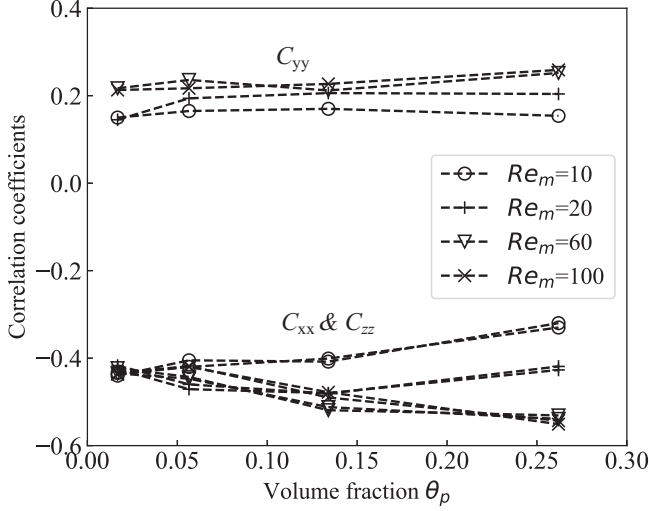


FIG. 11. Correlation coefficients between the nearest-neighbor distance and fluid-particle interaction

As a comparison, the coefficients  $B_1$  and  $B_2$  for the PFP stress are also listed in Table I. These values show that in the relative flow direction, the PFP stress is negligible compared to the Reynolds stress for the fluid motion, while in the directions perpendicular to the relative velocity, the PFP stress is about 15% to 45% of the Reynolds stress depending on the particle Reynolds number and the volume fraction. As mentioned above, since the effect of PFP stress is more important for the particle phase motion than for the fluid phase motion, as a future work, it will be interesting to compare the PFP stress to the Reynolds stress of the particle phase in the flows with moving particles.

#### D. An interesting correlation

The effect of the surrounding particles on the drag of a particle has been studied numerically. Although for a specified particle, knowing its nearest neighbor is not sufficient to approximate the drag on it [17,55], the influence of the nearest particle on the drag is still an interesting question to explore. For this purpose, we now study the correlation tensor

$$\mathbf{C}(\mathbf{x}) = \frac{\int (\mathbf{r} - \bar{\mathbf{r}}) (\bar{\mathbf{f}}_{\text{pf}}^{\text{nst}} - \bar{\mathbf{f}}_{\text{pf}}) P_{\text{nst}}(\mathbf{r} + \mathbf{x}|\mathbf{x}) d^3r}{\sqrt{\int |\mathbf{r} - \bar{\mathbf{r}}|^2 P_{\text{nst}}(\mathbf{r} + \mathbf{x}|\mathbf{x}) d^3r} \sqrt{\int |\bar{\mathbf{f}}_{\text{pf}}^{\text{nst}} - \bar{\mathbf{f}}_{\text{pf}}|^2 P_{\text{nst}}(\mathbf{r} + \mathbf{x}|\mathbf{x}) d^3r}}. \quad (28)$$

Similarly to (25), using (20) and noting that  $\nabla p_f$  is independent of  $\mathbf{r}$ , the force  $\mathbf{f}_{\text{pf}}$  above can be replaced with  $\mathbf{f}_h$ . Also as the discussion before (26), for statistically uniform particle distributions, one can replace the ensemble average  $\int (\cdot)^{\text{nst}} P_{\text{nst}}(\mathbf{r} + \mathbf{x}|\mathbf{x}) d^3r$  with  $\sum_{i=1}^{N_t} (\cdot) / N_t$ . We then write (28) as [56]

$$\mathbf{C}(\theta_p, Re_m) = \frac{N_t \sum_{i=1}^{N_t} (\mathbf{r}_i \mathbf{f}_{h,i}) - \sum_{i=1}^{N_t} \mathbf{r}_i \sum_{i=1}^{N_t} \mathbf{f}_{h,i}}{\sqrt{N_t \sum_{i=1}^{N_t} |\mathbf{r}_i|^2 - \left| \sum_{i=1}^{N_t} \mathbf{r}_i \right|^2} \sqrt{N_t \sum_{i=1}^{N_t} |\mathbf{f}_{h,i}|^2 - \left| \sum_{i=1}^{N_t} \mathbf{f}_{h,i} \right|^2}}. \quad (29)$$

For a uniform and isotropic particle distribution, with the mean fluid velocity in the  $y$  direction, the correlation tensor becomes  $\mathbf{C} = \text{diag}[C_{xx}, C_{yy}, C_{zz}]$ , with  $C_{xx} = C_{zz}$ . The results for these coefficients are plotted in Fig. 11, where the negative values are for  $C_{xx}$  and  $C_{zz}$ , and the positive values are for  $C_{yy}$ . Roughly speaking, these correlation coefficients imply that about 20% of the streamwise drag variations and 30% to 50% of the lateral force fluctuations are associated

with the position of the nearest particle. Noting that  $\bar{\mathbf{r}} = \mathbf{0}$ , and  $\mathbf{f}_{h,i}$  is the hydrodynamic force on particle  $i$  with the nearest particle at distance  $r_i$  away, the positive correlation coefficient  $C_{yy}$  in the streamwise direction implies that on average, a particle experiences a greater drag if  $r_{iy} > 0$ , or the nearest particle is downstream from particle  $i$ . In other words, a leading particle tends to experience a greater drag than a trailing particle. Similarly, the negative coefficients  $C_{xx}$  and  $C_{zz}$  imply that in the directions perpendicular to the flow, the force  $\mathbf{f}_{h,i}$  tends to be in the opposite direction of the nearest particle, meaning a repulsive force between the particles. This observation is in confirmation with the PFP stress calculated above.

## V. CONCLUSIONS

It has been known that interactions among particles in a multiphase flow not only affect the mean drag of the particles, but also cause relative motions among particles at the interparticle length scale [16]. Representing the effect of these relative motions in the Eulerian-Eulerian equations for multiphase flows has been challenging because of the long-range nature of the hydrodynamic interactions among the particles. In this work, this difficulty is avoided by using the nearest particle statistics [28,29] leading to the PFP stress.

Particle-resolved numerical simulations of flows past fixed arrays of particles are performed for particle Reynolds number less than 140 and particle volume fraction less than 30% using NEKIBM [47]. In addition to the calculation of the drag forces on particles, the numerical results are processed using the nearest particle statistics [28,29] to calculate and study the PFP stress. We have also developed a functional form of the stress with two coefficients. The coefficients are then determined using the numerical results.

For the simulated flows, the PFP stress in the streamwise direction causes attraction among the particles. Perpendicular to the flow, the stress pushes particles apart. This property of the PFP stress suggests that in the simulated flow regime, the PFP stress is a macroscopic representation of the interparticle scale drafting–kissing–tumbling mechanism. Using the numerical results, the fluid Reynolds stress is also calculated. It is found that in the directions perpendicular to the relative motion between the phases, the PFP stress is about 15% to 45% of the fluid Reynolds stress.

The simulations are limited to fixed array of spheres due to the numerical difficulty of tracking moving boundaries. More work is needed to extend the simulation to multiphase flows with moving particles.

## ACKNOWLEDGMENTS

The financial support is provided by Exascale Computing Program (ECP), the Joint DoD/DOE Munitions Program, and the Advanced Simulation and Computing (ASC) program under the auspices of the United States Department of Energy. Y.Y. and S.B. acknowledge support from the U.S. Department of Energy, National Nuclear Security Administration, Advanced Simulation and Computing Program, as a Cooperative Agreement under the Predictive Science Academic Alliance Program, under Contract No. DE-NA0002378, by the Office of Naval Research (ONR) as part of the Multidisciplinary University Research Initiatives (MURI) Program, under Grant No. N00014-16-1-2617.

## APPENDIX

In this Appendix we present an alternative derivation of the force decomposition (5) and the PFP stress avoiding abstract mathematics [28,29]. We start our derivation by noting that in definition (13) for  $\mathbf{f}_{\text{pm}}(\mathbf{x})$ , the position  $\mathbf{x}$  is not the location of a particle but the midpoint of the pairs. When we calculate the total particle–mean-field force by integration  $\int_V n_p \mathbf{f}_{\text{pm}} d^3x$  over a volume  $V$ , we sum over all the forces on the probable particle pairs with the midpoints inside the volume. For

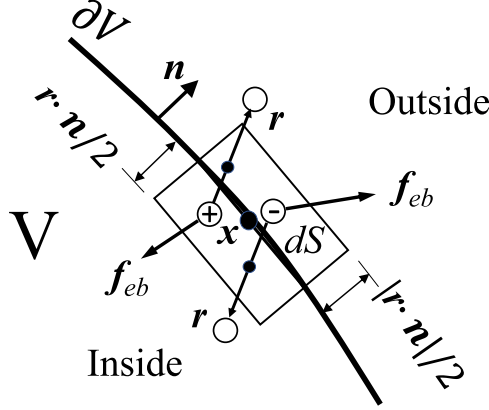


FIG. 12. Particle pairs across a boundary.

a sufficiently large volume, most of these pairs are within the volume. There are some boundary crossing pairs, as shown in Fig. 12. For the pairs with the midpoints outside  $V$ , the forces on the inside particle, such as the one marked with + in Fig. 12, are not included in  $\int_V n_p \bar{f}_{pm} d^3x$ . We call these particles type + particles. For the pairs with the midpoints inside, the forces on the outside particles, such as the one marked with - in Fig. 12, are included in the integral. We call these particles type - particles.

On the other hand, the total phase interaction forces  $\int_V n_p \bar{f}_{pr} d^3x$  in the volume  $V$  is calculated by summing over all the forces on the particles inside the volume. The difference between these total forces  $\int_V n_p \bar{f}_{pr} d^3x$  and  $\int_V n_p \bar{f}_{pm} d^3x$  comes from the boundary-crossing pairs. This difference is represented by the PFP stress as shown in the follows.

Suppose that we have calculated particle-mean-field force  $\int_V n_p \bar{f}_{pm} d^3x$  in the volume, to obtain the total phase interaction force  $\int_V n_p \bar{f}_{pr} d^3x$ , the forces on the type + particles need to be added, while the forces on the type - particles need to be subtracted off. Let  $dS$  be the surface element on the volume boundary  $\partial V$ . For pairs with distance vector  $\mathbf{r}$  between the particles, the region containing the type + particles is a layer with the thickness  $\frac{1}{2}\mathbf{r} \cdot \mathbf{n}$  inside the boundary  $\partial V$ , shown in Fig. 12 by the thin rectangle inside of the boundary, where  $\mathbf{n}$  is the unit outward normal. The volume of the region is  $\frac{1}{2}\mathbf{r} \cdot \mathbf{n} dS$ .

Since effective range of  $\mathbf{r}$  is  $O(\ell_p)$ , within an error of  $O(\ell_p/L)$ , we can approximate both the pair distribution function  $P_2$  and  $\mathbf{f}_{eb}$  as constants with values of  $P_2(\mathbf{x} - \mathbf{r}/2, \mathbf{x} + \mathbf{r}/2)$  and  $\mathbf{f}_{eb}(\mathbf{x} - \mathbf{r}/2, \mathbf{x} + \mathbf{r}/2)$  in the region. In this region the probable number of pairs with the distance vector at vicinity  $d^3r$  of  $\mathbf{r}$  is  $\frac{1}{2}\mathbf{r} \cdot \mathbf{n} dS P_2 d^3r$ . The total force on these particles is  $\frac{1}{2}\mathbf{f}_{eb} P_2 \mathbf{r} \cdot \mathbf{n} dS d^3r$ . Considering all possible distances between the particles in the pairs, we find the total force on type + particles near  $dS$  to be

$$\frac{1}{2} \int_{\mathbf{n} \cdot \mathbf{r} > 0} dS \mathbf{n} \cdot \mathbf{r} \mathbf{f}_{eb} P_2 d^3r, \quad (\text{A1})$$

where the integration domain restriction  $\mathbf{n} \cdot \mathbf{r} > 0$  is to ensure that the forces are on the inside particles with the other particle of the pair outside the volume. This force needs to be added to  $\int_V n_p \bar{f}_{pm} d^3x$ .

Similarly, the total force on the type - particles near  $dS$  is

$$\frac{1}{2} \int_{\mathbf{n} \cdot \mathbf{r} < 0} dS |\mathbf{n} \cdot \mathbf{r}| \mathbf{f}_{eb} P_2 d^3r, \quad (\text{A2})$$

where the integration domain restriction  $\mathbf{n} \cdot \mathbf{r} < 0$  is to ensure that the forces are on the outside particles with the other particle of the pair inside  $V$ . This force needs to be subtracted from  $\int_V n_p \mathbf{f}_{\text{pm}} d^3x$ . Combining (A1) and (A2), we have the total contribution from the boundary crossing pairs near  $dS$  as

$$\begin{aligned} \frac{1}{2} \left( \int_{\mathbf{n} \cdot \mathbf{r} > 0} dS \mathbf{n} \cdot \mathbf{r} - \int_{\mathbf{n} \cdot \mathbf{r} < 0} dS |\mathbf{n} \cdot \mathbf{r}| \right) \mathbf{f}_{\text{eb}} P_2 d^3r &= \frac{1}{2} \left( \int_{\mathbf{n} \cdot \mathbf{r} > 0} dS \mathbf{n} \cdot \mathbf{r} + \int_{\mathbf{n} \cdot \mathbf{r} < 0} dS \mathbf{n} \cdot \mathbf{r} \right) \mathbf{f}_{\text{eb}} P_2 d^3r \\ &= dS \mathbf{n} \cdot \frac{1}{2} \int \mathbf{r} \mathbf{f}_{\text{eb}} P_2 d^3r = dS \mathbf{n} \cdot \boldsymbol{\Sigma}_{\text{pfp}}. \end{aligned} \quad (\text{A3})$$

Since  $\mathbf{f}_{\text{eb}}(\mathbf{x} - \frac{\mathbf{r}}{2}, \mathbf{x} + \frac{\mathbf{r}}{2}) = \mathbf{f}_s(\mathbf{x}, \mathbf{r}) + \mathbf{f}_a(\mathbf{x}, \mathbf{r})$ , and  $\int \mathbf{r} \mathbf{f}_s P_2 d^3r = \mathbf{0}$  because of the symmetry in  $\mathbf{r}$ , similarly to the virial stress in molecular dynamics, the PFP stress only results from the antisymmetric forces between the particles.

With the such calculated contribution from the boundary crossing pairs on surface element  $dS$ , integrating this contribution from all the surface elements on volume  $V$ , we have

$$\int_V n_p \bar{\mathbf{f}}_{\text{pr}} d^3x = \int_V n_p \mathbf{f}_{\text{pm}} d^3x + \int_{\partial V} \mathbf{n} \cdot \boldsymbol{\Sigma}_{\text{pfp}} dS. \quad (\text{A4})$$

After the use of the Gauss theorem, we find (5).

- 
- [1] J. F. Richardson and W. N. Zaki, Sedimentation and fluidization: Part I, *Trans. Inst. Chem. Eng.* **32**, 35 (1954).
  - [2] M. Parmar, A. Haselbacher, and S. Balachandar, Generalized Basset-Boussinesq-Oseen Equation for Unsteady Forces on a Sphere in a Compressible Flow, *Phys. Rev. Lett.* **106**, 084501 (2011).
  - [3] P. Gualtieri, F. Picano, G. Sardina, and C. M. Casciola, Exact regularized point particle method for multiphase flows in the two-way coupling regime, *J. Fluid Mech.* **773**, 520 (2015).
  - [4] P. J. Ireland and O. Desjardins, Improving particle drag predictions in Euler-Lagrange simulations with two-way coupling, *J. Comput. Phys.* **338**, 405 (2017).
  - [5] T. Fukada, W. Fornari, L. Brandt, S. Takeuchi, and T. Kajishima, A numerical approach for particle-vortex interactions based on volume-averaged equations, *Int. J. Multiphase Flow* **104**, 188 (2018).
  - [6] J. Horwitz and A. Mani, Correction scheme for point-particle models applied to a nonlinear drag law in simulations of particle-fluid interaction, *Int. J. Multiphase Flow* **101**, 74 (2018).
  - [7] S. Balachandar, K. Liu, and M. Lakhote, Self-induced velocity correction for improved drag estimation in Euler-Lagrange point-particle simulations, *J. Comput. Phys.* **376**, 160 (2019).
  - [8] G. K. Batchelor, A new theory of the instability of a uniform fluidized bed, *J. Fluid Mech.* **193**, 75 (1988).
  - [9] R. O. Fox, A kinetic-based hyperbolic two-fluid model for binary hard-sphere mixtures, *J. Fluid Mech.* **877**, 282 (2019).
  - [10] R. O. Fox, F. Laurent, and A. Vié, A hyperbolic two-fluid model for compressible flows with arbitrary material-density ratios, *J. Fluid Mech.* **903**, A5 (2020).
  - [11] D. Lhuillier, Migration of rigid particles in non-brownian viscous suspensions, *Phys. Fluids* **21**, 023302 (2009).
  - [12] P. R. Nott, E. Guazzelli, and O. Pouliquen, The suspension balance model revisited, *Phys. Fluids* **23**, 043304 (2011).
  - [13] T. B. Anderson and R. Jackson, A fluid mechanical description of fluidized beds equations of motion, *Ind. Eng. Chem. Fundam.* **6**, 527 (1967).
  - [14] D. Z. Zhang and W. VanderHeyden, The effects of mesoscale structures on the macroscopic momentum equations for two-phase flows, *Int. J. Multiphase Flow* **28**, 805 (2002).
  - [15] Y. Igei and S. Sundaresan, Constitutive models for filtered two-fluid models of fluidized gas-particle flows, *Ind. Eng. Chem. Res.* **50**, 13190 (2011).

- [16] A. Fortes, D. Joseph, and T. Lundgren, Nonlinear mechanics of fluidization of beds of spherical particles, *J. Fluid Mech.* **177**, 467 (1987).
- [17] G. Akiki, W. Moore, and S. Balachandar, Pairwise-interaction extended point-particle model for particle-laden flows, *J. Comput. Phys.* **351**, 329 (2017).
- [18] G. K. Batchelor, Sedimentation in a dilute dispersion of spheres, *J. Fluid Mech.* **52**, 245 (1972).
- [19] G. K. Batchelor and J. T. Green, The determination of the bulk stress in a suspension of spherical particles to order  $c^2$ , *J. Fluid Mech.* **56**, 401 (1972).
- [20] D. J. Jeffrey, Conduction through a random suspension of spheres, *Proc. R. Soc. Lond. A* **335**, 355 (1973).
- [21] N. A. Patankar and D. D. Joseph, Modeling and numerical simulation of particulate flows by the Eulerian-Lagrangian approach, *Int. J. Multiphase Flow* **27**, 1659 (2001).
- [22] Z. Zhang and A. Prosperetti, A second-order method for three-dimensional particle simulation, *J. Comput. Phys.* **210**, 292 (2005).
- [23] E. Schlauch, M. Ernst, R. Seto, H. Briesen, M. Sommerfeld, and M. Behr, Comparison of three simulation methods for colloidal aggregates in Stokes flow: Finite elements, lattice Boltzmann and Stokesian dynamics, *Comput. Fluids* **86**, 199 (2013).
- [24] H. Tavassoli, E. Peters, and J. Kuipers, Direct numerical simulation of fluid-particle heat transfer in fixed random arrays of non-spherical particles, *Chem. Eng. Sci.* **129**, 42 (2015).
- [25] L. Wang, C. Peng, Z. Guo, and Z. Yu, Lattice Boltzmann simulation of particle-Laden turbulent channel flow, *Comput. Fluids* **124**, 226 (2016).
- [26] G. Akiki and S. Balachandar, Immersed boundary method with non-uniform distribution of lagrangian markers for a non-uniform Eulerian mesh, *J. Comput. Phys.* **307**, 34 (2016).
- [27] M. Wang, Y. Feng, T. Qu, S. Tao, and T. Zhao, Instability and treatments of the coupled discrete element and lattice Boltzmann method by the immersed moving boundary scheme, *Int. J. Numer. Methods Eng.* **121**, 4901 (2020).
- [28] D. Z. Zhang, Ensemble average and nearest particle statistics in disperse multiphase flows, *J. Fluid Mech.* **910**, A16 (2021).
- [29] D. Z. Zhang, Stress from long-range interactions in particulate systems, *Multiscale Model. Simul.* **19**, 1066 (2021).
- [30] J. H. Irving and I. G. Kirkwood, The statistical theory of transport processes. IV. The equations of hydrodynamics, *J. Chem. Phys.* **18**, 817 (1950).
- [31] D. Z. Zhang and A. Prosperetti, Averaged equations for inviscid disperse two-phase flow, *J. Fluid Mech.* **267**, 185 (1994).
- [32] D. Z. Zhang and A. Prosperetti, Momentum and energy equations for disperse two-phase flows and their closure for dilute suspensions, *Int. J. Multiphase Flow* **23**, 425 (1997).
- [33] D. Z. Zhang, W. B. VanderHeyden, Q. Zou, and N. T. Padiál-Collins, Pressure calculations in disperse and continuous multiphase flows, *Int. J. Multiphase Flow* **33**, 86 (2007).
- [34] J. T. Jenkins and S. B. Savage, A theory for the rapid flow of identical, smooth, nearly elastic, spherical particles, *J. Fluid Mech.* **130**, 187 (1983).
- [35] C. S. Campbell, The stress tensor for simple shear flows of a granular material, *J. Fluid Mech.* **203**, 449 (1989).
- [36] D. A. McQuarrie, Kinetic theory of gases and the Boltzmann equation, in *Statistical Mechanics* (Harper & Row, New York, 1976).
- [37] D. Z. Zhang, X. Ma, and R. M. Rauenzahn, Interspecies Stress in Momentum Equations for Dense Binary Particulate Systems, *Phys. Rev. Lett.* **97**, 048301 (2006).
- [38] S. Torquato, B. Lu, and J. Rubinstein, Nearest-neighbor function in many-body systems, *Phys. Rev. A* **41**, 2059 (1990).
- [39] S. Torquato, B. Lu, and J. Rubinstein, Nearest-neighbour distribution function for systems of interacting particles, *J. Phys. A: Math. Gen.* **23**, L103 (1990).
- [40] A. S. Sangani and A. K. Didwania, Dynamic simulations of flows of bubbly liquids at large Reynolds numbers, *J. Fluid Mech.* **250**, 307 (1993).
- [41] J. F. Brady and G. Bossis, Stokesian dynamics, *Ann. Rev. Fluid Mech.* **20**, 111 (1988).

- [42] S. Tenneti, R. Garg, and S. Subramaniam, Drag law for monodisperse gas–solid systems using particle-resolved direct numerical simulation of flow past fixed assemblies of spheres, *Int. J. Multiphase Flow* **37**, 1072 (2011).
- [43] M. Wang and D. Z. Zhang, Deformation accommodating periodic computational domain for a uniform velocity gradient, *Comput. Methods Appl. Mech. Eng.* **374**, 113607 (2021).
- [44] P. L. Barclay and D. Z. Zhang, Periodic boundary conditions for arbitrary deformations in molecular dynamics simulations, *J. Comput. Phys.* **435**, 110238 (2021).
- [45] G. J. Throop and R. J. Bearman, Numerical solutions of the Percus-Yevick equation for the hard-sphere potential, *J. Chem. Phys.* **42**, 2408 (1965).
- [46] A. T. Patera, A spectral element method for fluid dynamics: Laminar flow in a channel expansion, *J. Comput. Phys.* **54**, 468 (1984).
- [47] Y. Yang and S. Balachandar, A scalable parallel algorithm for direct-forcing immersed boundary method for multiphase flow simulation on spectral elements, *J. Supercomputing* **77**, 2897 (2020).
- [48] L. Schiller, A drag coefficient correlation, *Zeit. Ver. Deutsch. Ing.* **77**, 318 (1933).
- [49] J. Capecehatro and O. Desjardins, An Euler-Lagrange strategy for simulating particle-Laden flows, *J. Comput. Phys.* **238**, 1 (2013).
- [50] A. Seyed-Ahmadi and A. Wachs, Microstructure-informed probability-driven point-particle model for hydrodynamic forces and torques in particle-Laden flows, *J. Fluid Mech.* **900**, A21 (2020).
- [51] D. Z. Zhang and R. M. Rauenzahn, A viscoelastic model for dense granular flows, *J. Rheol.* **41**, 1275 (1997).
- [52] A. Biesheuvel and L. van Wijngaarden, Two-phase flow equations for a dilute dispersion of gas bubbles in liquid, *J. Fluid Mech.* **148**, 301 (1984).
- [53] M. Mehrabadi, S. Tenneti, R. Garg, and S. Subramaniam, Pseudo-turbulent gas-phase velocity fluctuations in homogeneous gas-solid flow: Fixed particle assemblies and freely evolving suspensions, *J. Fluid Mech.* **770**, 210 (2015).
- [54] W. C. Moore and S. Balachandar, Lagrangian investigation of pseudo-turbulence in multiphase flow using superposable wakes, *Phys. Rev. Fluids* **4**, 114301 (2019).
- [55] G. Akiki, T. L. Jackson, and S. Balachandar, Pairwise interaction extended point-particle model for a random array of monodisperse spheres, *J. Fluid Mech.* **813**, 882 (2017).
- [56] J. Benesty, J. Chen, Y. Huang, and I. Cohen, Pearson correlation coefficient, in *Noise Reduction in Speech Processing* (Springer, Berlin, 2009), pp. 1–4.